

Electronic and thermal effects in the insulator-metal phase transition in VO₂ nano-gap junctions

Arash Joushaghani,¹ Junho Jeong,¹ Suzanne Paradis,² David Alain,² J. Stewart Aitchison,¹ and Joyce K. S. Poon¹

¹Department of Electrical and Computer Engineering, University of Toronto, 10 King's College Road, Toronto, Ontario, M5S 3G4, Canada

²Defence Research and Development Canada - Valcartier, 2459 Pie-XI Blvd. North, Quebec, Quebec G3J 1X5, Canada

(Dated: 27 November 2014)

By controlling the thermal transport of VO₂ nano-gap junctions using device geometry, contact material, and applied voltage waveforms, the electronically induced insulator-metal phase transition is investigated in the adiabatic heating and transient carrier injection regimes. With a gradual ramping of an applied voltage on a microsecond time scale, the transition electric field threshold can be directly reduced by the Joule heating. With an abrupt applied voltage, the transition threshold is initiated by carriers injected within the first tens of nanoseconds, but the complete insulator-metal phase transition is limited by thermal redistribution times to hundreds of nanoseconds.

The dynamics of the insulator-metal phase transition (IMT) in the correlated electron material vanadium dioxide (VO₂)^{1,2} have attracted much attention^{3,4} due to potential application of VO₂ in transistors^{5,6} and opto-electronic^{7,8} switches. A reversible IMT through a structural reconfiguration occurs in VO₂ when the local temperature rises beyond the insulator-metal transition temperature, $T_{I \rightarrow M} = 340$ K⁹. This process takes place on the time scale of 10^{-7} - 10^{-5} s for nano-scale devices⁵. Alternatively, the IMT due to an electronic reconfiguration takes place on time scales of 10^{-12} - 10^{-8} s¹⁰ due to a perturbation in the electronic structure¹¹, accumulated surface charge¹², external strain¹³, applied electric fields or voltages¹⁴⁻¹⁸, and currents¹⁹. An electronically induced IMT produced by a current or applied voltages is typically accompanied by a local temperature increase in the VO₂ from Joule heating^{20,21}. The temperature rise modifies the temporal dynamics of the phase transition by inducing a secondary structural phase transition²¹ when the temperature exceeds $T_{I \rightarrow M}$. Although thermal effects can be reduced by limiting the current²² or increasing the heat dissipation rate of the devices²³, the role of Joule heating during an electronically induced IMT remains unclear^{5,24}.

In this Letter, we report the effects of heating on the electronically induced IMT in VO₂ nano-gap junctions. The thermal transport was controlled by the applied voltage waveform, device geometry, and metal contact. We studied the IMT in the adiabatic and transient regimes. The dependence of the IMT threshold voltage on the duration of the applied voltage pulses and device parameters can be explained by thermal accumulation and dissipation rates. The IMT could not occur in the absence of injected carriers, so carrier effects are critical in the electronically induced phase transition of VO₂.

The schematic and scanning electron micrograph (SEM) of the typical device are presented in Figs. 1(a)-1(b) respectively. A VO₂ film with a thickness of $h = 100$ nm was deposited using radio-frequency magnetron sputtering of a vanadium target on 2 μ m thermally grown layer of silica (SiO₂) on a silicon (Si) substrate. The VO₂ junctions were formed by a combination of electron beam (e-beam) lithography, metal evaporation, and lift-off to produce two metal contacts separated by a

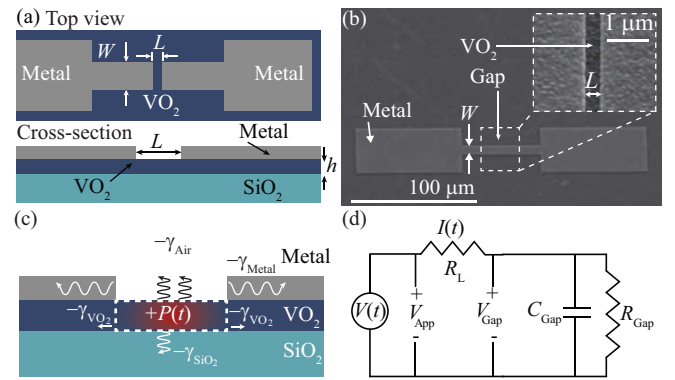


FIG. 1. (a) The top and side view schematic diagram of a VO₂ lateral junction. (b) SEM of the device and the magnified image of the gap. (c) The simplified model for the heat dissipation and generation mechanisms in the device. (d) The simplified circuit model of the device and the experiment.

gap of length L . These contacts had a width of $W = 10$ μ m and a thickness of $t = 100$ nm. The contacts were either gold (Au) or palladium (Pd).

The phase transition dynamics are limited by the RC time constant of the circuit, τ_{RC} , the thermal extraction time of the junction, τ_T , and the forward electronic phase transitions time constant, τ_E . An independent measurement of τ_E and τ_T of the junctions is difficult, since the electronic phase transition is typically accompanied with a temperature increase. As the temperature increases, the average electric field at the onset of the phase transition, $E_{I \rightarrow M}$, decreases²⁵ according to $E_{I \rightarrow M} \propto (1 - (T/T_c))^2$. However, by independently varying τ_T , we can evaluate the roles of the thermal and electronic effects, as well as their interaction in the phase transition.

The heat transfer channels in the VO₂ junction are illustrated in Fig. 1(c). The total heat dissipation rate of the junction is the sum of the effective heat extraction rates of the surrounding media, γ_x , where x is either air, VO₂, SiO₂ or the metal contact. Since the thermal conductivity of the contact metals is much larger than that of the VO₂, air, or SiO₂, the

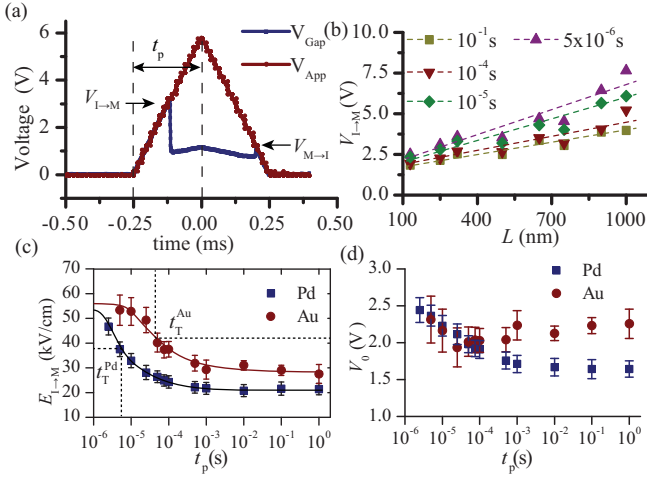


FIG. 2. (a) Time profiles of a V_{Gap} and V_{App} , when a triangular pulse with $t_p = 250 \mu\text{s}$ was applied. (b) The measured $V_{I \rightarrow M}$ as a function of L for pulses with different t_p . The measured (c) $E_{I \rightarrow M}$ and (d) V_0 as a function of t_p for devices with Pd or Au contacts.

total heat dissipation rate of the junction can be approximated as γ_{Metal} . The heat generation rate in the junction is the total dissipated electrical power, $P(t)$. As a result, the simplified heat transfer equation for the VO_2 junctions can be written as:

$$\rho_D C_p \frac{\partial T}{\partial t} = \kappa \nabla^2 T - \gamma_{\text{Metal}} T + \frac{P(t)}{\bar{V}_{\text{eff}}}, \quad (1)$$

where \bar{V}_{eff} is the effective volume of the junction, and ρ_D , C_p , and κ are the density, the specific heat capacity and the thermal conductivity of VO_2 respectively. This equation shows that γ_{Metal} and $P(t)$ changes the thermal transport time of the system and allows for the controlled study of τ_T and τ_E . In the experiments to follow, the contacts were either Au or Pd, and we controlled $P(t)$ by the applied voltage waveform. The thermal conductivities of Au and Pd are about $315 \text{ W/(m}\cdot\text{K)}$ and $70 \text{ W/(m}\cdot\text{K)}$, respectively.

To measure the time constants of the VO_2 devices, an arbitrary function generator was used to apply a voltage, V_{App} , across the device contacts and a series resistor $R_L = 550 \Omega$. The simplified circuit model of the device and the experiment is shown in Fig. 1(d). The voltage drop across the gap, V_{Gap} , and V_{App} were monitored using an oscilloscope. The measured τ_{RC} for the setup was $\approx 40 \pm 10 \text{ ns}$ and remained constant within the experimental error range for devices with different values of gap lengths and contact metals.

We investigated the adiabatic Joule heating regime by applying a periodic train of triangular voltage pulses, which gradually increased I and V_{Gap} and allowed sufficient time for Joule heating to occur. The rise time of the pulses, t_p , was at least $5 \mu\text{s}$. The period was 2 s to prevent cumulative heating from successive pulses. Figure 2(a) shows an example of the measured V_{Gap} and V_{App} . The phase transition manifested in a drop in V_{Gap} at the forward phase transition voltage $V_{I \rightarrow M}$, and an increase in V_{Gap} at the reverse transition voltage, $V_{M \rightarrow I}$.

To extract the electric field for the phase transition, we measured $V_{I \rightarrow M}$ for devices with different L and took the slopes of to be the “average” transition electric field, $E_{I \rightarrow M}$. The voltage offset, V_0 , taken to be the value of $V_{I \rightarrow M}$ as $L \rightarrow 0$, is due to the finite contact resistance and work function mismatch between VO_2 and the contact material. As an example, Figure 2(b) shows the measured $V_{I \rightarrow M}$ as a function of L for devices with Pd contacts and for t_p between $5 \mu\text{s}$ and 1 s . For all device lengths, shorter voltage pulses required higher values of $V_{I \rightarrow M}$, which meant more energy had to be deposited to the device to initiate the transition. This could be caused by a reduction of thermal accumulation (which would have decreased $V_{I \rightarrow M}$) and/or a limitation due to τ_E .

To investigate thermal influence on $E_{I \rightarrow M}$, we extracted $E_{I \rightarrow M}$ as a function of t_p for devices with Au or Pd metal contacts in Fig. 2(c). The solid lines are fits to guide the eye. For both types of samples, $E_{I \rightarrow M}$ was constant when $t_p \gtrsim 1 \text{ ms}$. As t_p decreased, $E_{I \rightarrow M}$ increased and saturated at around 55 kV/cm for the Au samples when $t_p < 10^{-5} \text{ s}$. $E_{I \rightarrow M}$ did not saturate for the Pd samples for the measured values of t_p . We define a characteristic pulse width, t_T , as the value of t_p that resulted in a 50% increase in $E_{I \rightarrow M}$ from its value at $t_p = 1 \text{ s}$. As shown in Fig. 2(c), $t_T^{\text{Au}} \approx 3 \times 10^{-5} \text{ s}$ for the Au samples and $t_T^{\text{Pd}} \approx 5 \times 10^{-6} \text{ s}$ for the Pd samples.

The dependence of $E_{I \rightarrow M}$ on t_p and the contact metal can be explained by thermal transport. When $t_p \gg t_T$, Joule heating raised the temperature in the VO_2 junction, which reduced $E_{I \rightarrow M}$. As t_p decreased, heating had a lesser contribution and consequently $E_{I \rightarrow M}$ increased. Since Au has a higher thermal conductivity than Pd (which would reduce the temperature of the VO_2 in the Au samples), $E_{I \rightarrow M}$ for Au was larger than in the Pd samples at all values of t_p . $E_{I \rightarrow M}$ saturated when $t_p \ll t_T$, which was approximately the value of $E_{I \rightarrow M}$ when no thermal effects were present. In the Au samples, the saturation of $E_{I \rightarrow M}$ to about 55 kV/cm when $t_p \ll t_T$ occurred when almost no thermal effects were present. This field value agrees well with measurements of vertical VO_2 junctions, in which heat accumulation is minimized owing to large device cross-sections²⁷.

The temperature change in the VO_2 due to the applied voltage further affects the carrier density in the devices. Fig. 2(d) shows the offset voltage, V_0 , vs. t_p . Both the carrier density²⁸ and the work function²⁹ of VO_2 increase across the phase transition with a similar temperature dependence as $E_{I \rightarrow M}$ ²⁵. However, while a higher carrier density reduces V_0 , a higher work function increases V_0 . The carrier density effects tend to dominate over the work function changes, because the carrier density can change by about 3 orders of magnitude across the IMT, while the work function changes by less than 3%²⁹. The measured resistivity change of the junctions was slightly larger than 2 orders of magnitude²³. Therefore, the increase in V_0 when $t_p < t_T$, in a similar way as $E_{I \rightarrow M}$ in Fig. 2(c), suggests the carrier density decreased as the voltage pulses became shorter and the role of heating was reduced.

To study the IMT without thermal effects, we applied square-wave pulses with rise time $t_p \ll t_T$, which was limited to 40 ns due to the experimental setup. The pulses had a duration of $1 \mu\text{s}$ and a period of 2 s . The amplitude of V_{App} ,

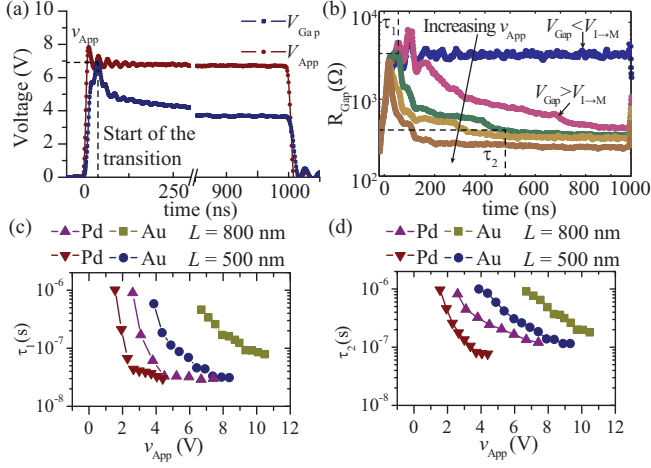


FIG. 3. (a) The measured V_{App} and V_{Gap} when a square-wave pulse with a duration of $1 \mu\text{s}$ was applied across the devices. (b) The measured resistance of the device as V_{Gap} increased. The measured (c) τ_1 and (d) τ_2 of the devices vs. the applied voltage amplitude.

v_{App} , was varied and the time profile of V_{Gap} was measured. Figure 3(a) shows an example of the measured V_{App} and V_{Gap} , and v_{App} is indicated. As before, the drop in V_{Gap} indicated the start of the phase transition. The value of $E_{I \rightarrow M}$ was determined using the smallest value of v_{App} that triggered the IMT for each L and was 52 ± 5 kV/cm for Pd and 55 ± 8 kV/cm for Au devices. These values agreed well with the saturation values of $E_{I \rightarrow M}$ in Fig. 2(c).

Figure 3(b) shows the measured values of R_{Gap} as v_{App} increased for a device with $L = 800$ nm and Pd contacts. R_{Gap} was constant when $V_{\text{Gap}} < V_{I \rightarrow M}$. Increasing v_{App} such that $V_{\text{Gap}} \geq V_{I \rightarrow M}$ resulted in a rapid drop in R_{Gap} at a time of τ_1 after the rise of the pulse. R_{Gap} continued to decrease and dropped below 10 dB of its initial value at τ_2 after the rise of the pulse. Both τ_1 and τ_2 decreased with increasing v_{App} . Figures 3(c)-3(d) show the measured τ_1 and τ_2 as a function of v_{App} for devices with two different values of L and contact metals. As v_{App} increased, τ_1 for the $L = 500$ nm Pd and Au devices and $L = 800$ nm Pd devices decreased and saturated at approximately τ_{RC} . This suggests τ_1 is due to the combined effects of τ_{RC} and τ_{E} with $\tau_{\text{E}} \leq \tau_{\text{RC}}$. τ_1 did not saturate for the $L = 800$ nm Au device for the voltages tested. τ_2 also decreased with increasing v_{App} at a lower rate than τ_1 , consistent with τ_2 being caused by Joule heating of the VO_2 . As expected, longer channels required more time for the heat to redistribute. For the same device length and the same voltage difference from the phase transition threshold, τ_2 for Au was higher than that for Pd by up to a factor of about 2, because the local temperature of the Au samples would be lower owing to the higher thermal conductivity of Au. As v_{App} , or equivalently, the applied electrical power, increased, τ_2 decreased because of the faster rate of heating as described by Eq. 1.

These measurements confirm that the phase transition is initiated electronically and occurs on a timescale limited by the RC time constant of the measurement setup, and is followed by a thermal transition that is limited by the thermal dissipa-

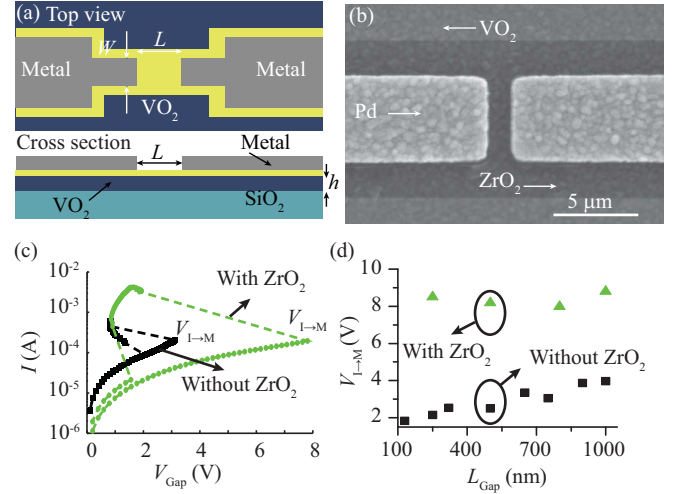


FIG. 4. (a) The top and side view schematics of a VO_2 lateral junction with a dielectric insulating layer. (b) SEM image of the device at the gap. The contrast of the ZrO_2 has been enhanced using an X-ray detector. (c) The IV characteristics of device with $L = 500$ nm. The measured data are marked by the dots, and the dashed lines connect the data across the phase transition. (d) The measured $V_{I \rightarrow M}$ vs. L for devices with and without the ZrO_2 layer.

tion of the junction. To suppress the thermal effects, it is essential to reduce I by electrically insulating the VO_2 from the metallic contacts. One approach is to use a thin high- k dielectric between the VO_2 and the metallic contacts. Figure 4(a) shows the schematic of the device. A 7 nm thick layer of zirconium dioxide (ZrO_2) was deposited using atomic layer deposition and patterned using a combination of electron beam lithography and lift-off. The metal contacts were formed as before using Pd and had the width of $W = 10 \mu\text{m}$ and thickness of 100 nm. Figure 4(b) is an X-ray enhanced SEM image of the device near the gap showing that the thin dielectric layer that covers the VO_2 surface.

To observe the phase transition, we measured V_{Gap} and the current, I , that leaked through the ZrO_2 and VO_2 layers. Figure 4(c) shows the measured IV characteristics of two junctions with (green) and without (black) the ZrO_2 layer. Both devices had the same $L = 500$ nm. The current, I , initially increased with increasing V_{Gap} and the phase transition resulted in a drop in V_{Gap} . As expected, the ZrO_2 layer reduced I by an order of magnitude at any value of V_{Gap} . However, the ZrO_2 layer also increased $V_{I \rightarrow M}$ by a factor of 2.5, which resulted in a value of I that was similar to devices without ZrO_2 . Figure 4(d) shows the measured $V_{I \rightarrow M}$ vs. L for devices with (green) and without (black) the ZrO_2 layer. $V_{I \rightarrow M}$ did not change with L for devices with the ZrO_2 layer, indicating that the phase transition occurred due to the electric field breakdown of the ZrO_2 that allowed sufficient current to pass through the device before the phase transition occurred.

As another approach to limit the current, we fabricated VO_2 nano- and micro-wires placed between a capacitor with an air gap. The VO_2 wires were fabricated using e-beam lithography and subsequent reactive ion etching. The metal contacts

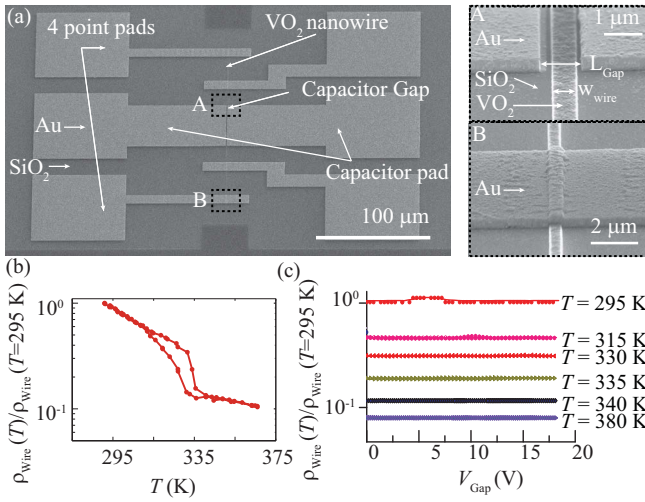


FIG. 5. (a) SEM images of the device, VO₂ nanowire in the capacitor gap, and metal contact. (b) The normalized resistivity of the wire. (c) The wire resistivity as a function of V_{Gap} at different temperatures.

were defined using e-beam lithography, thermal evaporation of 400 nm of Au, and a subsequent lift-off step. Figure 5(a) shows the SEM images of the fabricated device and the magnified images, showing the VO₂ nanowire at the gap and on the metal contacts. Four metal pads contacted the VO₂ wire to accurately measure the wire resistivity, ρ_{Wire} . A voltage of V_{Gap} was applied across the capacitor, which established an electric field in a section of the VO₂ between the electrodes.

Figure 5(b) shows the normalized resistivity of the wire $\rho_{\text{Wire}}(T)/\rho_{\text{Wire}}(T = 295 \text{ K})$ as a function of T for a wire with a width of 500 nm and a thickness of 100 nm. When $T > 335 \text{ K}$, the VO₂ underwent a phase transition and the resistivity of the wires dropped. Figure 5(c) shows the normalized resistivity as V_{Gap} increased. The resistivity did not change with V_{Gap} up to the breakdown voltage of the gap, which was about 20 V. Below the breakdown voltage, the leakage current remained less than 10 pA. The measurements were repeated at different temperatures to decrease the required $E_{I \rightarrow M}$. Even when $T \approx T_{I \rightarrow M}$, the normalized resistivity was unaffected by V_{Gap} . As previously mentioned, the required electric field for the phase transition of VO₂ scales as $1/T$ and is $< 5 \text{ kV/cm}$ close to $T_{I \rightarrow M}$. According to finite element simulations, the average electric field in these devices was $> 10 \text{ kV/cm}$. However, these electric field values did not result in any detectable changes in ρ_{Wire} even at elevated temperatures. If an external electric field could induce a phase transition in these films, its threshold would have been $\gg 10 \text{ kV/cm}$, a value which was not achieved in this experiment. Consequently, we conclude that the most plausible cause of the phase transition in these films was carrier injection.

In summary, we have shown the influence of Joule heating on the threshold electric field, carrier densities, and phase transition time scales of the IMT in micro- and nano-scale two terminal VO₂ junctions. The phase transition was initiated by carrier injection (not electric field). The measured thermal dis-

sipation time was 10^{-7} s , while the measured electronic transition time was limited by the RC time constant of the setup to 40 ns. The thermal effects can be suppressed using high frequency circuits for current regulation after the phase transition. These circuits are typically used for current quenching in avalanche photodiodes³⁰ and can be potentially adapted to VO₂ devices.

- ¹D. N. Basov, R. D. Averitt, D. van der Marel, M. Dressel, and K. Haule, *Reviews of Modern Physics* **83**, 471 (2011).
- ²Y. Zhou and S. Ramanathan, *Critical Reviews in Solid State and Materials Sciences* **38**, 286 (2013).
- ³A. Cavalleri, C. Toth, C. W. Siders, J. A. Squier, F. Raksi, P. Forget, and J. C. Kieffer, *Physical Review Letters* **87**, 237401 (2001).
- ⁴S. Lysenko, V. Vikhnin, A. Ra, F. Fernandez, and H. Liu, *Physical Review B* **82**, 205425 (2010).
- ⁵S. D. Ha, Y. Zhou, C. J. Fisher, S. Ramanathan, and J. P. Treadway, *Journal of Applied Physics* **113**, 184501 (2013).
- ⁶Z. Yang, C. Ko, and S. Ramanathan, *Annual Review of Materials Research* **41**, 337 (2011).
- ⁷A. Joushaghani, B. A. Kruger, S. Paradis, D. Alain, J. Stewart Aitchison, and J. K. S. Poon, *Applied Physics Letters* **102**, 061101 (2013).
- ⁸B. A. Kruger, A. Joushaghani, and J. K. S. Poon, *Optics Express* **20**, 23598 (2012).
- ⁹C. N. Berglund, *Electron Devices*, *IEEE Transactions on* **16**, 432 (1969).
- ¹⁰K. Appavoo, B. Wang, N. F. Brady, M. Seo, J. Nag, R. P. Prasankumar, D. J. Hilton, S. T. Pantelides, and R. F. Haglund, *Nano Letters* **14**, 1127 (2014).
- ¹¹Z. Tao, T.-R. T. Han, S. D. Mahanti, P. M. Duxbury, F. Yuan, C.-Y. Ruan, K. Wang, and J. Wu, *Physical Review Letters* **109**, 166406 (2012).
- ¹²M. Nakano, K. Shibuya, D. Okuyama, T. Hatano, S. Ono, M. Kawasaki, Y. Iwasa, and Y. Tokura, *Nature* **487**, 459 (2012).
- ¹³J. Cao, E. Ertekin, V. Srinivasan, W. Fan, S. Huang, H. Zheng, J. W. L. Yim, D. R. Khanal, D. F. Ogletree, J. C. Grossman, and J. Wu, *Nat Nano* **4**, 732 (2009).
- ¹⁴G. Stefanovich, A. Pergament, and D. Stefanovich, *Journal of Physics: Condensed Matter* **12**, 8837 (2000).
- ¹⁵D. Ruzmetov, G. Gopalakrishnan, C. Ko, V. Narayanamurti, and S. Ramanathan, *Journal of Applied Physics* **107**, 114516 (2010).
- ¹⁶W. W. Peng, G. Niu, R. Tetot, B. Vilquin, F. Raimondi, J. B. Brubach, E. Amzallag, T. Yanagida, S. Autier-Laurent, P. Lecoeur, and P. Roy, *Journal of Physics: Condensed Matter* **25**, 445402 (2013).
- ¹⁷Z. You, C. Xiaonan, K. Changhyun, Y. Zheng, C. Mouli, and S. Ramanathan, *Electron Device Letters*, *IEEE* **34**, 220 (2013).
- ¹⁸A. Kar, N. Shukla, E. Freeman, H. Paik, H. Liu, R. Engel-Herbert, S. S. N. Bharadwaja, D. G. Schlom, and S. Datta, *Applied Physics Letters* **102**, 072106 (2013).
- ¹⁹T. Driscoll, J. Quinn, M. Di Ventra, D. N. Basov, G. Seo, Y.-W. Lee, H.-T. Kim, and D. R. Smith, *Physical Review B* **86**, 094203 (2012).
- ²⁰A. Zimmers, L. Aigouy, M. Mortier, A. Sharoni, S. Wang, K. G. West, J. G. Ramirez, and I. K. Schuller, *Physical Review Letters* **110**, 056601 (2013).
- ²¹S. Kumar, M. D. Pickett, J. P. Strachan, G. Gibson, Y. Nishi, and R. S. Williams, *Advanced Materials* **25**, 6128 (2013).
- ²²B. Simon Mun, J. Yoon, S.-K. Mo, K. Chen, N. Tamura, C. Dejoie, M. Kunz, Z. Liu, C. Park, K. Moon, and H. Ju, *Applied Physics Letters* **103**, 061902 (2013).
- ²³A. Joushaghani, J. Jeong, S. Paradis, D. Alain, J. Stewart Aitchison, and J. K. S. Poon, *Applied Physics Letters* **104**, 221904 (2014).
- ²⁴Y. Zhang and S. Ramanathan, *Solid-State Electronics* **62**, 161 (2011).
- ²⁵A. L. Pergament, P. P. Boriskov, A. A. Velichko, and N. A. Kuldin, *Journal of Physics and Chemistry of Solids* **71**, 874 (2010).
- ²⁶S. B. Lee, K. Kim, J. S. Oh, B. Kahng, and J. S. Lee, *Applied Physics Letters* **102**, 063501 (2013).
- ²⁷Z. Yang, S. Hart, C. Ko, A. Yacoby, and S. Ramanathan, *Journal of Applied Physics* **110**, 033725 (2011).
- ²⁸D. Ruzmetov, D. Heiman, B. B. Claffin, V. Narayanamurti, and S. Ramanathan, *Physical Review B* **79**, 153107 (2009).
- ²⁹C. Ko, Z. Yang, and S. Ramanathan, *ACS Applied Materials and Interfaces* **3**, 3396 (2011).
- ³⁰S. Cova, M. Ghioni, A. Lacaita, C. Samori, and F. Zappa, *Applied Optics* **35**, 1956 (1996).